Analysis and Design of Current Control Schemes for *LCL*-Type Grid-Connected Inverter Based on a General Mathematical Model

Donghua Pan, *Member, IEEE*, Xinbo Ruan, *Fellow, IEEE*, Xuehua Wang, *Member, IEEE*, Hui Yu, and Zhongwei Xing

***Abstract*—For the *LCL*-type grid-connected inverter, there are basically three current control schemes, namely the grid current control, the inverter-side inductor current control, and the weighted average current control. This paper builds a general mathematical model to describe the three current control schemes. In this model, the grid current is an equivalent target control variable, the capacitor current feedback serves as a damping solution, and the computation and pulse-width modulation delays are taken into account. Based on the general mathematical model, a comparative analysis of different control schemes is carried out in terms of the grid current stability. It reveals that when the inverter-side inductor current is controlled, the grid current shows the same stability as the inverter-side inductor current; but when the weighted average current is controlled, both the grid current and the inverter-side inductor current are critically stable even though the weighted average current can be easily stabilized. Moreover, the general mathematical model also provides a unified perspective to design different control schemes, which makes the controller parameter tuning more straightforward and effective. In this way, a set of controller parameters which yields high robustness against the grid-impedance variation can be selected for all the three current control schemes. Finally, a 6-kW prototype is built, and experiments are performed to verify the theoretical analysis.**

***Index Terms*—Active damping, current control, general mathematical model, grid-connected inverter, *LCL* filter.**

NOMENCLATURE

V_{in}	DC input voltage.
v_{inv}	Inverter bridge output voltage.
v_C	Filter capacitor voltage.
v_g, V_g	Grid voltage and its RMS value.
V_{tri}	Amplitude of the triangular carrier.
i_{L1},i_{L1}^*	Inverter-side inductor current and its reference.
i_C	Filter capacitor current.
i_{L2},i_{L2}^*	Grid current and its reference.
i_{WA},i_{WA}^*	Weighted average current and its reference.
β	Weight value of inverter-side inductor current.
$1-\beta$	Weight value of grid current.
L_1	Inverter-side inductor of an *LCL* filter.
C	*LCL* filter capacitor.
L_2	Grid-side inductor of an *LCL* filter.
L_g	Grid inductance.
f_o	Fundamental frequency.
f_r	*LCL*-filter resonance frequency.
f_s	Sampling frequency.
f_{sw}	Switching frequency.
ω_o	Fundamental angular frequency, $\omega_o = 2\pi f_o$.
ω_r	*LCL*-filter resonance angular frequency, $\omega_r = 2\pi f_r$
T_s	Sampling period, $T_s = 1/f_s$.

Manuscript received October 29, 2015; revised February 9, 2016, April 19, 2016, and July 10, 2016; accepted August 11, 2016. Date of publication August 24, 2016; date of current version February 11, 2017. This work was supported by the National Natural Science Foundation of China under Award 50837003 and by the Jiangsu Province 333 Program for Excellent Talents under Award BRA2012141. Recommended for publication by Associate Editor M. Liserre.

D. Pan, X. Wang, H. Yu, and Z. Xing are with the State Key Laboratory of Advanced Electromagnetic Engineering and Technology, School of Electrical and Electronic Engineering, Huazhong University of Science and Technology, Wuhan 430074, China (e-mail: pan_dh@hust.edu.cn; wang.xh@hust.edu.cn; hyu11@ncsu.edu; xingzhw@hust.edu.cn).

X. Ruan is with the State Key Laboratory of Advanced Electromagnetic Engineering and Technology, School of Electrical and Electronic Engineering, Huazhong University of Science and Technology, Wuhan 430074, China, and also with the Center for More-Electric-Aircraft Power Systems, College of Automation Engineering, Nanjing University of Aeronautics and Astronautics, Nanjing 210016, China (e-mail: ruanxb@nuaa.edu.cn).

Color versions of one or more of the figures in this paper are available online at http://ieeexplore.ieee.org.

Digital Object Identifier 10.1109/TPEL.2016.2602219

I. INTRODUCTION

WITH the increase of energy demand, there is a growing interest in distributed power generation systems (DPGS). As an interface between DPGS and a power grid, a grid-connected inverter plays an important role in injecting high-quality power into the grid [1]. In the grid-connected inverter, an output filter is needed to attenuate the switching harmonics. Compared with an *L* filter, an *LCL* filter is considered to be a preferred option for its higher attenuating ability. However, due to the resonance hazard of the *LCL* filter, damping solutions are required to stabilize the system [2]. To avoid the attendant power loss with passive damping [3]–[5], active damping solutions are proposed with specific control algorithms [6]–[8]. Among various active damping solutions, the capacitor-current-feedback active damping has been widely used for its ease of implementation [9]–[11].

In addition to the resonance damping, current control is another important issue for the *LCL*-type grid-connected inverter. Unlike the *L* filter where the inductor current is the only control variable, the *LCL* filter offers more alternatives. In the *LCL*-type grid-connected inverter, any of the grid current, the

inverter-side inductor current, and their weighted average value can be controlled. Grid current control has the advantage of directly controlling the power injected into the grid, which is convenient to set the power factor on the grid side [12]–[14]. Inverter-side inductor current control is beneficial to the instantaneous overcurrent protection for the inverter [15]–[17]. Particularly, if the grid current and the inverter-side inductor current are properly weighted, and the weighted average current is fed back as the target control variable, then the control system will be degraded from three-order to first-order. This helps to simplify the design procedure of the current regulator [18]–[20].

Recent literatures have paid much attention to the analysis and design of the aforementioned three current control schemes, particularly when the computation and pulse-width modulation (PWM) delays are taken into account. Owing to the digital delays, the system stability will depend on the ratio of the *LCL*-filter resonance frequency f_r to the sampling frequency f_s. With a typical delay of one and half sampling periods, the critical resonance frequency is proved to be $f_s/6$ [21]–[23]. If $f_r < f_s/6$, the inverter- side inductor current feedback alone can stabilize the system without damping, while the grid current feedback cannot, thus the inverter-side inductor current control is superior to the grid current control; if $f_r > f_s/6$, the stability situation is just the opposite, and the grid current control is more advantageous [24]–[26]. Apparently, the critical resonance frequency can be intentionally arranged by optimizing the delay time. For example, if the overall delay is reduced to one sampling period, the critical resonance frequency will be raised to $f_s/4$ [25], [26]. Therefore, for a specific resonance frequency range, a single current feedback is enough to guarantee a stable operation. While, in practice, the *LCL*-filter resonance frequency will vary in a wide range due to the variation of grid impedance [27], and it might cross over the critical frequency. Under such circumstance, an additional damping is still required to achieve a strong robustness. In [28], the inverter-side inductor current is controlled, and a positive feedback of the capacitor current is introduced to improve the system stability at a high resonance frequency. However, the mechanism how the positive feedback of capacitor current works is not well reported. In [29], the grid current is controlled, and the capacitor-current-feedback active damping is evaluated. It reveals that due to the computation and PWM delays, the damping performance behaves as a negative resistor which can easily cause instability. To overcome this drawback, the capacitor-current- feedback methods with reduced or compensated computation delay are proposed in [29]–[32]. Moreover, based on the work in [29], an optimized controller design is presented in [33] to achieve high robustness against the grid-impedance variation.

Despite the extensive literatures that have been published on the subject, the connections and differences among the three current control schemes remain not fully revealed, since these control schemes are modeled and analyzed independently. In the independent models, each control scheme focuses on the stability of its own target control variable and uses it as a criterion to evaluate its control performance. Thus, the three control schemes are separately evaluated by three different criteria. This can cover up the shortcomings of these control schemes and is not proper for comparing their performances. A fair comparison should be made on the basis of a common evaluation criterion. In fact, although various currents can be used as the target control variable, the final output of the *LCL*-type grid-connected inverter is always the grid current. Therefore, the *stability of grid current* should be a basic criterion to evaluate the performance levels of the three control schemes. However, in the inverter-side inductor current control and the weighted average current control, it is inexplicit to tell the stability of grid current since the grid current is indirectly controlled. In these indirect current control schemes, their target control variables are the intermediate outputs of the system. From a control perspective, a stable intermediate variable can still lead to an unstable final output [34]. As is claimed in [35], when the inverter-side inductor current is controlled to be stable, undesirable oscillation may arise in the grid current due to the resonance between the grid-side inductor and the filter capacitor. In view of this, it is necessary to reexamine the two indirect current control schemes in terms of the grid current stability.

This paper is dedicated to addressing this issue. A general mathematical model is firstly built in this paper to describe the three current control schemes for the *LCL*-type grid-connected inverter. In this model, the grid current is an equivalent target control variable, the capacitor current feedback serves as a damping solution, and the computation and PWM delays are taken into account. With the general mathematical model, the three current control schemes can be depicted with a single structure, which focuses on the stability of grid current and allows these control schemes to be analyzed on a comparable basis. Moreover, the general mathematical model also provides a unified perspective to design different control schemes, which makes the controller parameter tuning more straightforward and effective. Based on this model, the stability analysis and controller design drawn from the grid current control, which have been discussed in [29]–[33], can be directly applied to the other two current control schemes. In this way, the stability of grid current can be explicitly judged, and the controller parameters yielding strong robustness can be easily picked out, for all the three current control schemes.

This paper is organized as follows. In Section II, the three current control schemes of the *LCL*-type grid-connected inverter are briefly reviewed at first, and then, through equivalent transformation of their control block diagrams, a general mathematical model is constructed. Based on this model, a comparative analysis of different control schemes is carried out in terms of the grid current stability in Section III. Meanwhile, a further explanation from the circuit level is presented in this section to help understand the theoretical analysis. In Section IV, a unified design procedure for the controller parameters, which takes account of the grid-impedance variation, is proposed using the general mathematical model. In Section V, a 6-kW prototype of a single-phase *LCL*-type grid-connected inverter is built, and experimental results are provided to confirm the theoretical expectations. Finally, Section VI concludes this paper.

II. General Mathematical Model of the *LCL*-Type Grid-Connected Inverter

Fig. 1 shows the configuration of a single-phase voltage-source inverter feeding into the grid through an *LCL* filter. L_1 is

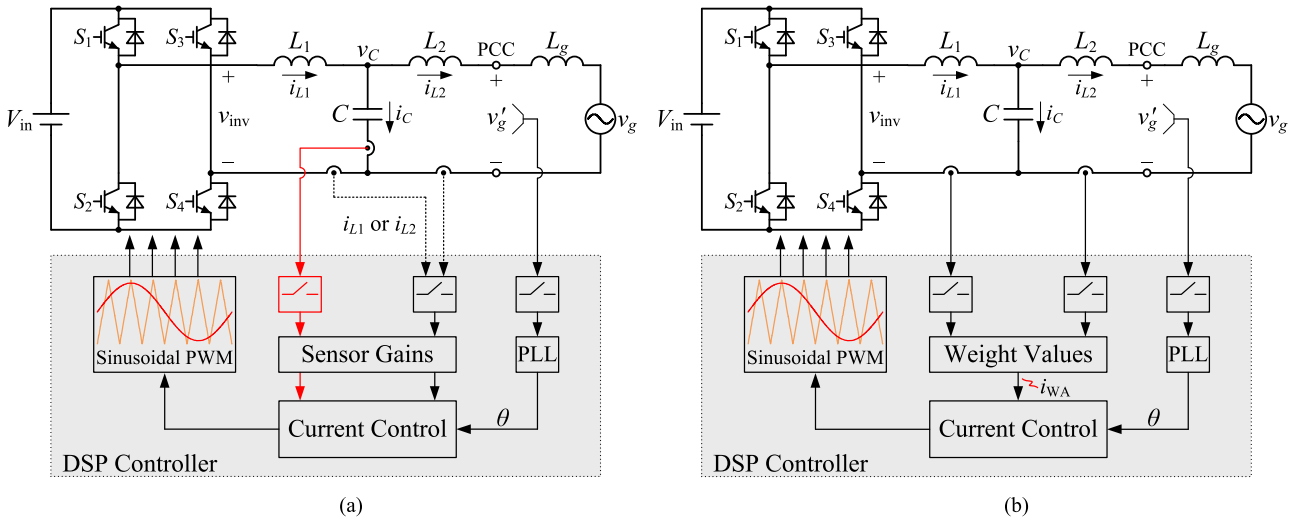

Fig. 1. Topology and current control architectures of an *LCL*-type grid-connected inverter. (a) Grid current control and inverter- side inductor current control. (b) Weighted average current control.

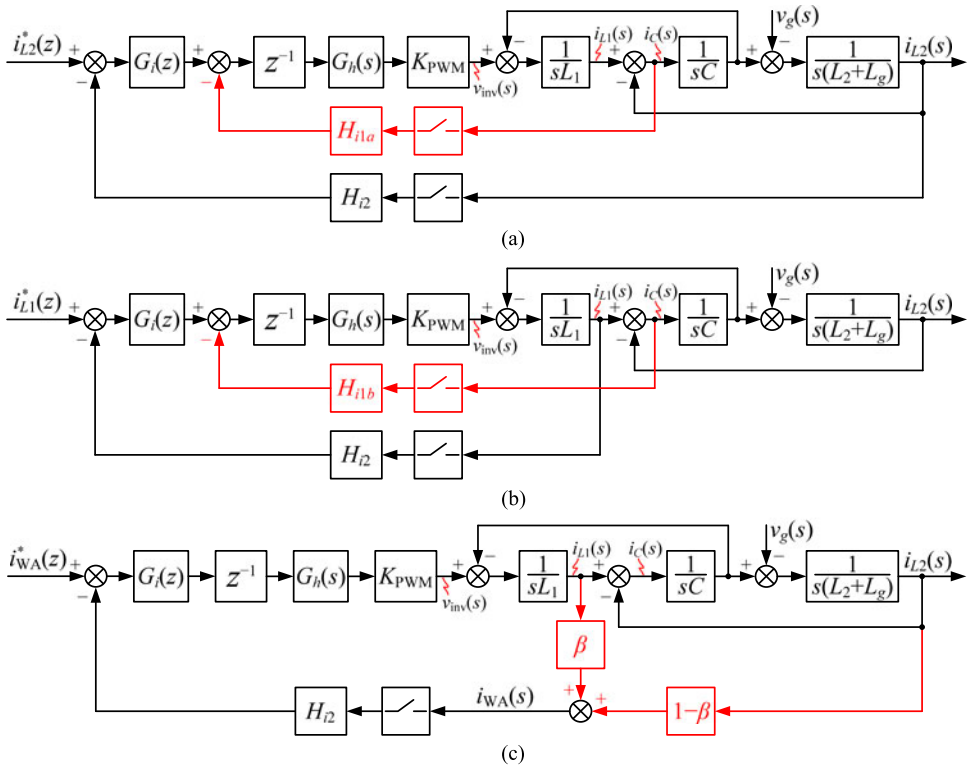

Fig. 2. Mathematical models of (a) grid current control, (b) inverter-side inductor current control, and (c) weighted average current control.

the inverter-side inductor, C is the filter capacitor, and L_2 is the grid-side inductor. Generally, the grid impedance at the point-of-common coupling (PCC) consists of inductance and resistance [27]. Since the grid resistance offers some damping and helps stabilize the system, a pure inductance L_g is considered here to draw the worst case.

In the *LCL*-type grid-connected inverter, the grid current i_{L2}, the inverter-side inductor current i_{L1}, or their weighted average value i_{WA} can be controlled. When i_{L1} or i_{L2} is controlled, an additional feedback of the capacitor current i_{C} is needed to actively damp the *LCL*-filter resonance [28], [29], as shown in Fig. 1(a). Fig. 1(b) shows that of the weighted average current control, in which both i_{L1} and i_{L2} are sampled and properly weighted, and the weighted average current i_{WA} is fed to the current controller [18]–[20]. From Fig. 1, it is clear to see that all the three control schemes employ two current sensors, and the current sensors in the weighted average current control are relatively expensive since the measured currents are both

of high values. Irrespective of the applied control variables, a phase-locked loop (PLL) is used to extract the phase angle of the voltage at the PCC, which is denoted by v_g', so that i_{L2} can be synchronized with v_g'. To help investigate the three current control schemes, a discrete-time modeling that accounts for the computation and PWM delays is deduced as follows.

A. Grid Current Control

Fig. 2(a) shows the mathematical model of the grid current control with capacitor-current-feedback active damping. $i_{L2}^{*}(z)$ is the grid current reference, $v_{\text{inv}}(s)$ is the inverter bridge output voltage, and $G_i(z)$ is the current regulator. The computation and PWM delays, with a total value of one and half sampling periods, are incorporated in this model. Specifically, the computation delay is one sampling period in the widely used synchronous sampling scheme [36]–[38] and it is modeled as z^{-1}. The PWM delay is half sampling period, and it is caused by the zero-order hold (ZOH) effect, which is expressed as

$$G_h(s) = \frac{1 - e^{-sT_s}}{s} \tag{1}$$

where T_s is the sampling period. K_{PWM} is the transfer function of the PWM inverter and expressed as

$$K_{\text{PWM}} = \frac{V_{\text{in}}}{V_{\text{tri}}} \tag{2}$$

where V_{in} is the input voltage, and V_{tri} is the amplitude of the triangular carrier. H_{i1a} is the feedback coefficient of i_C, and H_{i2} is the sensor gain of i_{L1} and i_{L2}.

B. Inverter-Side Inductor Current Control

For the inverter-side inductor current control with capacitor-current-feedback active damping, its mathematical model is shown in Fig. 2(b), where $i_{L1}^{*}(z)$ is the inverter-side inductor current reference. To differ from Fig. 2(a), the feedback coefficient of i_C is denoted by H_{i1b} here. By discretizing Fig. 2(b), the system discrete loop gain $T_{iL1}(z)$ can be obtained. The rigorous derivation of this loop gain is presented in Appendix. Here, its expression is given as (3) as shown at the bottom of the page.

Since i_{L1} is the target control variable in Fig. 2(b), its stability can be easily judged by applying the Nyquist stability criterion to $T_{iL1}(z)$. For convenience of illustration, $T_{iL1}(z)$ is called the loop gain of i_{L1} here. In (3), ω_r is the resonance angular frequency of the *LCL* filter and expressed as

$$\omega_r = \sqrt{\frac{L_1 + L_2 + L_g}{L_1 (L_2 + L_g) C}} \tag{4}$$

and the resonance frequency is $f_r = \omega_r / (2\pi)$.

C. Weighted Average Current Control

The mathematical model of the weighted average current control is shown in Fig. 2(c), where $i_{\text{WA}}^{*}(z)$ is the weighted average current reference, and β and $1-\beta$ are the weight values of i_{L1} and i_{L2}, respectively. By discretizing Fig. 2(c), the system discrete loop gain $T_{i\text{WA}}(z)$, which is derived in the Appendix, can be obtained as (5) as shown at the bottom of the page.

Similarly, $T_{i\text{WA}}(z)$ is the loop gain of i_{WA}. From (5), it can be found that if β is equal to

$$\beta = \frac{L_1}{L_1 + L_2 + L_g} \tag{6}$$

then there will be a pair of pole-zero cancellations in $T_{i\text{WA}}(z)$. Thus, $T_{i\text{WA}}(z)$ can be simplified as

$$T_{i\text{WA}}(z) = \frac{H_{i2} K_{\text{PWM}} T_s G_i(z)}{z(z-1)(L_1 + L_2 + L_g)}. \tag{7}$$

From (7), it is obvious that $T_{i\text{WA}}(z)$ is the same as the loop gain of the *L*-type grid-connected inverter with $L = L_1 + L_2 + L_g$ [24]. That means by adopting the weighted average current control with $\beta = L_1/(L_1 + L_2 + L_g)$, the control system is degraded from three-order to first-order, thus its target control variable i_{WA} can be easily stabilized [18]–[20].

D. General Mathematical Model

From the above analysis, it is worth noting that in the inverter-side inductor current control and the weighted average current control, the grid current is indirectly controlled. Therefore, the mathematical models depicted in Fig. 2(b) and (c), and their corresponding loop gains $T_{iL1}(z)$ and $T_{i\text{WA}}(z)$ can only be, respectively, used to judge the stability of i_{L1} and i_{WA}, rather than that of i_{L2}. In order to assess the grid current stability, an equivalent model with i_{L2} being the target control variable would be desirable.

Referring to Fig. 2(b), considering that $i_{L1} = i_{L2} + i_C$, the feedback of i_{L1} can be divided into two parts, namely the feedback of i_{L2} and the feedback of i_C. By moving the feedback

$$T_{iL1}(z) = \frac{H_{i2} K_{\text{PWM}} G_i(z)}{\omega_r L_1 (L_1 + L_2 + L_g)} \cdot \frac{\omega_r L_1 T_s \left(z^2 - 2z\cos\omega_r T_s + 1\right) + (z-1)^2 (L_2 + L_g) \sin\omega_r T_s}{(z-1)\left[z(z^2 - 2z\cos\omega_r T_s + 1) + \frac{H_{i1b} K_{\text{PWM}}}{\omega_r L_1}(z-1)\sin\omega_r T_s\right]}. \tag{3}$$

$$T_{i\text{WA}}(z) = \frac{H_{i2} K_{\text{PWM}} G_i(z)}{\omega_r L_1 (L_1 + L_2 + L_g)} \cdot \frac{\omega_r L_1 T_s \left(z^2 - 2z\cos\omega_r T_s + 1\right) + (z-1)^2 \left[\beta(L_1 + L_2 + L_g) - L_1\right] \sin\omega_r T_s}{z(z-1)(z^2 - 2z\cos\omega_r T_s + 1)} \tag{5}$$

$$T_{iL2}(z) = \frac{H_{i2} K_{\text{PWM}} G_i(z)}{\omega_r (L_1 + L_2 + L_g)} \cdot \frac{\omega_r T_s \left(z^2 - 2z\cos\omega_r T_s + 1\right) - (z-1)^2 \sin\omega_r T_s}{(z-1)\left[z(z^2 - 2z\cos\omega_r T_s + 1) + \frac{K_{\text{PWM}} \sin\omega_r T_s}{\omega_r L_1}(z-1) H_{i1}(z)\right]} \tag{8}$$

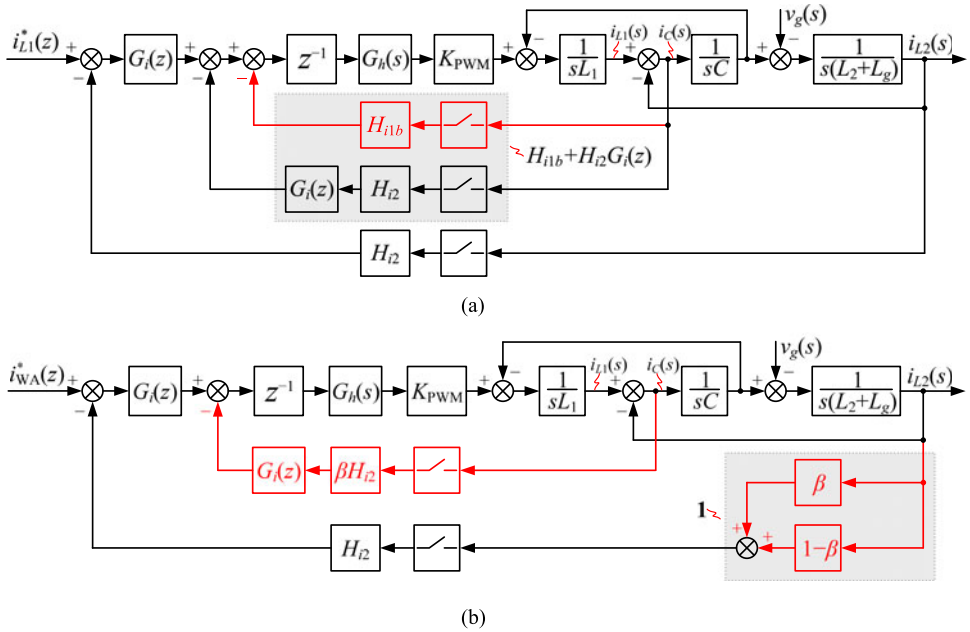

Fig. 3. Equivalent transformations of the mathematical models for (a) inverter-side inductor current control and (b) weighted average current control.

node of i_C to the output of $G_i(z)$, an equivalent block diagram is obtained, as shown in Fig. 3(a). It is clear to see that controlling i_{L1} can be regarded as controlling i_{L2} with a capacitor-current-feedback active damping, and its feedback function is $H_{i2}G_i(z)$. Since this part of damping comes along with the feedback of i_{L1}, it is called the inherent damping. Combining this inherent damping with the additional capacitor-current-feedback path, the overall damping term is obtained as $H_{i1b} + H_{i2}G_i(z)$. The inherent damping feature for the inverter-side inductor current control has been found in [39], but its damping performance is evaluated in the continuous domain where the delay effect is not considered. As is proved in [29]–[33], the digital delays have substantial impacts on the capacitor-current-feedback active damping and the overall system stability and they cannot be ignored. Therefore, it is necessary to reexamine the inherent damping performance in the discrete domain to find some new features for the digitally controlled system.

Similarly, recalling Fig. 2(c), by dividing the feedback of i_{L1} into the feedback of i_{L2} and the feedback of i_C, and moving the feedback node of i_C to the output of $G_i(z)$, an equivalent block diagram is also obtained, as shown in Fig. 3(b). It can be seen that the inherent capacitor-current-feedback function in the weighted average current control is $\beta H_{i2}G_i(z)$.

Previous analysis shows that whether i_{L2} is directly or indirectly controlled, the control systems can all be described in a general form, as shown in Fig. 4, in which i_{L2} is the equivalent target control variable, $i_{\text{ref}}(z)$ is the current reference, and the capacitor current feedback serves as a damping solution with $H_{i1}(z)$ being the feedback function. The expressions of $i_{\text{ref}}(z)$ and $H_{i1}(z)$ for the specific control schemes are listed in Table I.

Different from the models depicted in Fig. 2(b) and (c), the general mathematical model takes i_{L2} as the equivalent target control variable; thus, it can be used to judge the stability of i_{L2} for different current control schemes. By discretizing Fig. 4, the system discrete loop gain $T_{iL2}(z)$, which is derived in the Appendix, can be obtained as equation (8) as shown at the bottom of the previous page.

TABLE I
EQUIVALENCE OF DIFFERENT CURRENT CONTROL SCHEMES

Current control schemes	$i_{\text{ref}}(z)$	$H_{i1}(z)$	Simplified H_{i1}
Grid current control	$i_{L2}^*(z)$	H_{i1a}	H_{i1a}
Inverter-side inductor current control	$i_{L1}^*(z)$	$H_{i1b} + H_{i2}G_i(z)$	$H_{i1b} + H_{i2}K_p$
Weighted average current control	$i_{\text{WA}}^*(z)$	$\beta H_{i2}G_i(z)$	$\beta H_{i2}K_p$

Accordingly, $T_{iL2}(z)$ is the loop gain of i_{L2}. Substituting (8) into the characteristic equation $1 + T_{iL2}(z) = 0$ and manipulating, the characteristic polynomial of i_{L2}, i.e., $P_{iL2}(z)$, is obtained as

$$\begin{aligned} P_{iL2}(z) = {} & \omega_r L_1 (z^2 - 2z\cos\omega_r T_s + 1)[z(z-1) \\ & \times (L_1 + L_2 + L_g) + H_{i2}K_{\text{PWM}}T_s G_i(z)] \\ & + K_{\text{PWM}} \sin\omega_r T_s (z-1)^2 [(L_1 + L_2 + L_g) \\ & \times H_{i1}(z) - L_1 H_{i2} G_i(z)]. \end{aligned} \tag{9}$$

The closed-loop poles of i_{L2} can be determined by solving $P_{iL2}(z) = 0$. Note that $P_{iL2}(z)$ is general to all the three control schemes, it will be used to analyze the grid current stability in the following section.

III. Indirect Current Control Schemes Reanalyzed in Terms of Grid Current Stability

Based on the general mathematical model depicted in Section II, the two indirect current control schemes, i.e., the inverter-side inductor current control and the weighted average current control are reanalyzed in terms of the grid current stabil-

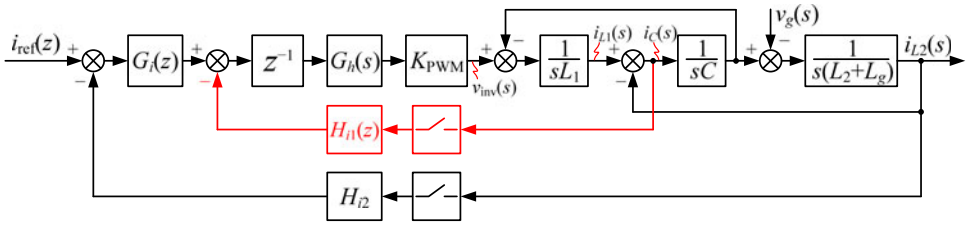

Fig. 4. General mathematical model of the digitally controlled *LCL*-type grid-connected inverter.

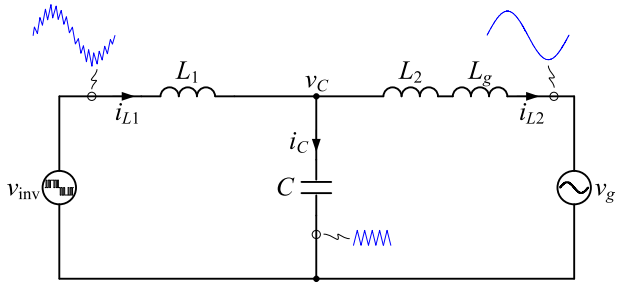

Fig. 5. Simplified circuit of the *LCL*-type grid-connected inverter.

ity in this section. Afterward, a comparison of the three current control schemes is drawn to help understand the connections and differences among them.

A. Inverter-Side Inductor Current Control

Recalling the analysis in Section II-B, substituting the loop gain $T_{iL1}(z)$, which is given in (3), into the characteristic equation $1 + T_{iL1}(z) = 0$ and manipulating, the characteristic polynomial of i_{L1}, i.e., $P_{iL1}(z)$, is obtained as

$$\begin{aligned} P_{iL1}(z) = {} & \omega_r L_1 (z^2 - 2z\cos\omega_r T_s + 1)[z(z-1) \\ & \times (L_1 + L_2 + L_g) + H_{i2} K_{\mathrm{PWM}} T_s G_i(z)] \\ & + K_{\mathrm{PWM}} \sin\omega_r T_s (z-1)^2 [(L_1 + L_2 + L_g) \\ & \times H_{i1b} + (L_2 + L_g) H_{i2} G_i(z)]. \end{aligned} \tag{10}$$

As shown in Table I, for the inverter-side inductor current control, $H_{i1}(z) = H_{i1b} + H_{i2}G_i(z)$. Substituting it into (9), and considering (10), it can be found that $P_{iL2}(z) = P_{iL1}(z)$. That means, when i_{L1} is controlled, the closed-loop poles of i_{L2} are the same as those of i_{L1}. Hence, the stabilities of i_{L2} and i_{L1} are the same. In other words, i_{L2} is definitely stable once i_{L1} has been stabilized and *vice versa*. This finding corrects the assumption in [35] that i_{L2} may be unstable when i_{L1} is stabilized. To make a more intuitive sense, a further explanation from the circuit level is presented as follows.

Fig. 5 shows the simplified circuit of the *LCL*-type grid-connected inverter, where the inverter bridge output voltage v_{inv} is represented by a voltage source. If i_{L1} is controlled to be stable, there will be fundamental component and switching harmonics in both v_{inv} and i_{L1}. The switching harmonics in i_{L1} are bypassed by the filter capacitor branch, which leaves the fundamental current to be injected into the grid. It is worth noting that no resonance arises between $(L_2 + L_g)$ and C in this case. This is because that if there is a resonance, the resonant voltage of C will be applied on L_1, which surely gives rise to the current oscillation in i_{L1} and results in instability. Likewise, if i_{L2} is controlled to be stable, there is also no resonance between L_1 and C. From this point of view, L_1 or $(L_2 + L_g)$ alone cannot resonate with C, and the resonance will definitely take place among all the three components of the *LCL* filter.

B. Weighted Average Current Control

In the weighted average current control, there are two situations depending on the value of β. If $\beta \neq L_1/(L_1 + L_2 + L_g)$, substituting the loop gain $T_{i\mathrm{WA}}(z)$, which is given in (5), into the characteristic equation $1 + T_{i\mathrm{WA}}(z) = 0$ and manipulating, the characteristic polynomial of i_{WA}, i.e., $P_{i\mathrm{WA}}(z)$, is obtained as

$$\begin{aligned} P_{i\mathrm{WA}}(z) = {} & \omega_r L_1 (z^2 - 2z\cos\omega_r T_s + 1)[z(z-1) \\ & \times (L_1 + L_2 + L_g) + H_{i2} K_{\mathrm{PWM}} T_s G_i(z)] \\ & + K_{\mathrm{PWM}} \sin\omega_r T_s (z-1)^2 [\beta(L_1 + L_2 + L_g) \\ & - L_1] H_{i2} G_i(z). \end{aligned} \tag{11}$$

As shown in Table I, for the weighted average current control, $H_{i1}(z) = \beta H_{i2} G_i(z)$. Substituting it into (9) and considering (11), it can be found that $P_{iL2}(z) = P_{i\mathrm{WA}}(z)$. That means, when i_{WA} is controlled with $\beta \neq L_1/(L_1 + L_2 + L_g)$, the closed-loop poles of i_{L2} are the same as those of i_{WA}. Therefore, the stabilities of i_{L2} and i_{WA} are the same in this case.

If $\beta = L_1/(L_1 + L_2 + L_g)$, substituting the loop gain $T_{i\mathrm{WA}}(z)$, which is given in (7), into the characteristic equation $1 + T_{i\mathrm{WA}}(z) = 0$ and manipulating, the characteristic polynomial $P_{i\mathrm{WA}}(z)$ is obtained as

$$P_{i\mathrm{WA}}(z) = z(z-1)(L_1 + L_2 + L_g) + H_{i2} K_{\mathrm{PWM}} T_s G_i(z). \tag{12}$$

Again, substituting $H_{i1}(z) = \beta H_{i2} G_i(z)$ and $\beta = L_1/(L_1 + L_2 + L_g)$ into (9) and considering (12), $P_{iL2}(z)$ can be rewritten as

$$\begin{aligned} P_{iL2}(z) &= \omega_r L_1 (z^2 - 2z\cos\omega_r T_s + 1)[z(z-1) \\ &\quad \times (L_1 + L_2 + L_g) + H_{i2} K_{\mathrm{PWM}} T_s G_i(z)] \\ &= \omega_r L_1 (z^2 - 2z\cos\omega_r T_s + 1) P_{i\mathrm{WA}}(z). \end{aligned} \tag{13}$$

From (13), it is clear to see that for $\beta = L_1/(L_1 + L_2 + L_g)$, $P_{iL2}(z)$ is the multiplication of $P_{i\mathrm{WA}}(z)$ and a second-order polynomial $\omega_r L_1 (z^2 - 2z\cos\omega_r T_s + 1)$. That means the

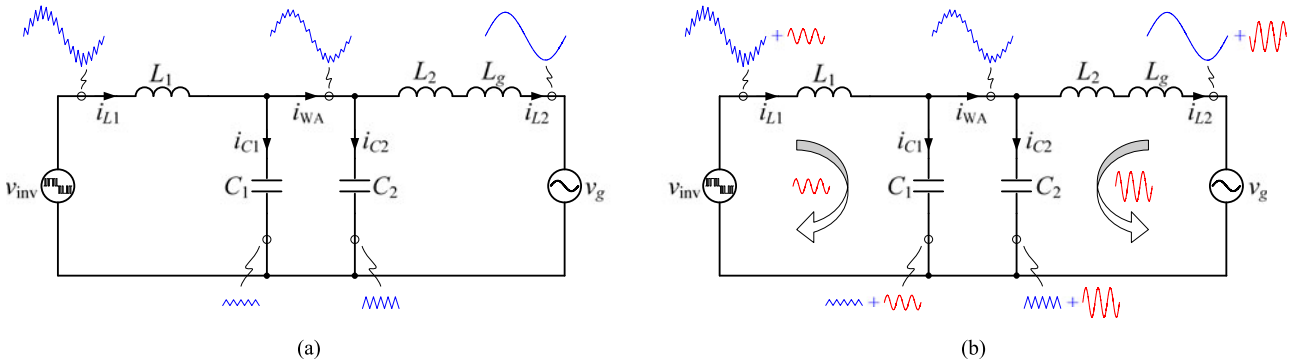

Fig. 6. Simplified circuit of the *LCL*-type grid-connected inverter with weighted average current control. (a) $\beta \neq L_1/(L_1 + L_2 + L_g)$. (b) $\beta = L_1/(L_1 + L_2 + L_g)$.

closed-loop poles of i_{L2} have one more pair added to those of $i_{\rm WA}$. Solving the equation z^2–$2z\cos\omega_{\rm r}T_{\rm s}$+1 = 0, the additional closed-loop poles are obtained as

$$z_{1,2} = e^{\pm j\omega_r T_s} = \cos\omega_r T_s \pm j\sin\omega_r T_s. \tag{14}$$

From (14), it is obvious that $|z_{1,2}| = 1$, which means $z_{1,2}$ is a pair of resonant poles located at the unit circle, and its resonance frequency is exactly the *LCL*-filter resonance frequency f_r. Due to this pair of resonant poles, i_{L2} can only be *critically stable* even though $i_{\rm WA}$ has been stabilized. Recalling the analysis in Section III-A, i_{L1} is also critically stable in this case since the stabilities of i_{L1} and i_{L2} are the same. Similarly, this stability feature can be explained with the system simplified circuit.

Fig. 6 shows the simplified circuit of the *LCL*-type grid-connected inverter with weighted average current control. According to the definition of the weighted average current, the following equation can be obtained:

$$\begin{aligned} i_{\rm WA} &= \beta i_{L1} + (1-\beta) i_{L2} = \beta(i_{L2} + i_C) \\ &\quad + (1-\beta) i_{L2} = i_{L2} + \beta i_C. \end{aligned} \tag{15}$$

From (15), it is clear to see that $i_{\rm WA}$ is the summation of i_{L2} and a part of the capacitor current βi_C, where βi_C can be obtained by splitting the filter capacitor. If C is split into C_1 and C_2 by

$$C_1 = (1-\beta)\, C,\ C_2 = \beta C \tag{16}$$

then $i_{C1} = (1-\beta) i_C$ and $i_{C2} = \beta i_C$, where i_{C1} and i_{C2} are the currents of C_1 and C_2, respectively. Thus, $i_{\rm WA}$ can be rewritten as

$$i_{\rm WA} = i_{L2} + \beta i_C = i_{L2} + i_{C2}. \tag{17}$$

Observing (17) and Fig. 6, it can be found that $i_{\rm WA}$ is exactly the current flowing between C_1 and C_2.

Referring to Fig. 6, it can be seen that there are two resonant loops, which are composed of $L_1 - C_1$ and $(L_2 + L_g) - C_2$ separately. According to (16), their resonance frequencies are calculated as

$$\begin{aligned} f_{r1} &= \frac{1}{2\pi\sqrt{L_1 C_1}} = \frac{1}{2\pi\sqrt{(1-\beta)\, L_1 C}}, \\ f_{r2} &= \frac{1}{2\pi\sqrt{(L_2 + L_g)\, C_2}} = \frac{1}{2\pi\sqrt{\beta\,(L_2 + L_g)\, C}}. \end{aligned} \tag{18}$$

From (18), it is obvious that for $\beta \neq L_1/(L_1+L_2+L_{\rm g})$, $f_{r1} \neq f_{r2}$; and for $\beta = L_1/(L_1+L_2+L_{\rm g})$, the following equation can be obtained:

$$f_{r1} = f_{r2} = \frac{1}{2\pi}\sqrt{\frac{L_1 + L_2 + L_g}{L_1\,(L_2 + L_g)\, C}} \triangleq f_r. \tag{19}$$

Recalling Fig. 6(a), if $i_{\rm WA}$ is controlled to be stable for $\beta \neq L_1/(L_1 + L_2 + L_g)$, then there will be no resonances in both $L_1 - C_1$ and $(L_2 + L_{\rm g}) - C_2$. This is because that if there is a resonance, the resonances of $L_1 - C_1$ and $(L_2 + L_g) - C_2$ cannot take place separately since $f_{r1} \neq f_{r2}$, and a part of resonant current will definitely transfer between the two resonant loops, which surely gives rise to the current oscillation in $i_{\rm WA}$ and results in instability. However, for $\beta = L_1/(L_1 + L_2 + L_g)$, separate resonances will arise in $L_1 - C_1$ and $(L_2 + L_g) - C_2$ even though $i_{\rm WA}$ is stabilized, as shown in Fig. 6(b). This is because that the two resonant loops formed by $L_1 - C_1$ and $(L_2 + L_g) - C_2$ are independent since $f_{r1} = f_{r2}$, and the resonant current will only circulate inside each resonant loop instead of transferring between them. Accordingly, the resonant components will be added to i_{L1}, i_{C1}, i_{C2}, and i_{L2}, rather than $i_{\rm WA}$ ($i_{\rm WA}$ contains the fundamental component and a part of switching harmonics), and the resonant currents in i_{L1} and i_{L2} are out of phase. From this point of view, when adopting the weighted average current control with $\beta = L_1/(L_1 + L_2 + L_g)$, the resonance will disappear in $i_{\rm WA}$ but still exist in i_{L1} and i_{L2}.

C. Comparison of the Three Current Control Schemes

In the previous sections, the three current control schemes are described in a general mathematical model, with the grid current being the equivalent target control variable and the capacitor current feedback being the damping solution. Based on this model, the two indirect current control schemes have been

reanalyzed in terms of the grid current stability. From the above analysis, the connections and differences among the three current control schemes can be summarized as follows.

1) From the perspective of grid current, the differences among the three current control schemes lie in two aspects, i.e., the current reference (or the target control variable) and the capacitor-current-feedback function, as shown in Table I. It is the different damping terms that lead to the different stabilities of the grid current.
2) The inherent damping exists in both the inverter-side inductor current control and the weighted average current control. The inherent damping in the inverter-side inductor current control helps to stabilize the grid current for $f_r < f_s/6$, but it destabilizes the grid current for $f_r > f_s/6$ (see Section IV); the inherent damping in the weighted average current control makes the grid current critically stable for $\beta = L_1/(L_1 + L_2 + L_g)$.
3) The control system is of three-order in both the grid current control and the inverter-side inductor current control, whereas the control system is degraded to first-order in the weighted average current control with $\beta = L_1/(L_1 + L_2 + L_g)$. Essentially, the reduction of control order does not show any real advantage since it has an implicit resonance hazard, as shown in Fig. 6(b).

From the general mathematical model, it can be foreseen that if different control schemes are designed with identical current regulator $G_i(z)$ and capacitor-current-feedback function $H_{i1}(z)$, i.e., matched-loop gain $T_{iL2}(z)$, the same control performance and stability will be resulted. This property will be verified by a design example given in the following section.

IV. Unified Controller Design With the General Mathematical Model

The general mathematical model is not only an effective method to analyze the different current control schemes, but also a promising way to design them. Since all the three current control schemes are described in a single model, there is no need to perform a separate design for each control scheme. Based on the general mathematical model, the controller parameters of the three control schemes are designed in a unified way in this section. The grid impedance is considered in this design. To deal with the wide-range variation of grid impedance, an optimized controller design has been proposed in [33] for the grid current control. Fortunately, the general mathematical model also takes the grid current as the equivalent target control variable. Therefore, the design procedure in [33] can be directly applied to different control schemes based on the general mathematical model.

Table II gives the parameters of a 6-kW single-phase *LCL*-type grid-connected inverter, where the unipolar sine-triangle, asymmetrical regular sampled PWM is implemented. The *LCL* filter is designed with the well-known constraints, i.e., the inverter-side current ripple is less than 30% (peak-to-peak) of the rated fundamental current, the capacitive reactive power is less than 5% of the rated load, and the grid-side switching harmonic is less than 0.3% of the rated fundamental current [40]–[42]. The consequent resonance frequency is $f_r = 4.6$ kHz. The controller parameters are designed for this filter setting, and the system stability is examined with L_g varying up to 10% per unit, which corresponds to 2.6 mH in the test system.

TABLE II
Parameters of the Prototype

Parameter	Symbol	Value	Parameter	Symbol	Value
Input voltage	V_{in}	360 V	Inverter-side inductor	L_1	600 μH
Grid voltage (RMS)	V_g	220 V	Grid-side inductor	L_2	150 μH
Output power	P_o	6 kW	Filter capacitor	C	10 μF
Fundamental frequency	f_o	50 Hz	Resonance frequency	f_r	4.6 kHz
Switching frequency	f_{sw}	10 kHz	Sampling frequency	f_s	20 kHz
Amplitude of the triangular carrier	V_{tri}	4.58 V	Current sensor gain	H_{i2}	0.15

Referring to Fig. 4, a unified design of the current regulator $G_i(z)$ and the capacitor-current-feedback function $H_{i1}(z)$ is deduced as follows. A proportional-resonant (PR) regulator is employed as the current regulator, and it is intentionally kept the same for different current control schemes. In the *s*-domain, PR regulator is expressed as

$$G_i(s) = K_p + \frac{2K_r\omega_i s}{s^2 + 2\omega_i s + \omega_o^2} \tag{20}$$

where $\omega_o = 2\pi f_o$ is the fundamental angular frequency, and ω_i is the resonant cut off frequency. In view of a typical $\pm 1\%$ variation of the grid fundamental frequency [27], $\omega_i = 1\% \cdot 2\pi f_o = \pi$ rad/ s is set. The proportional gain K_p and resonant gain K_r are tuned considering the overall system dynamics which are evaluated by the crossover frequency f_c and the phase margin (PM). Specifically, K_p is related to f_c by [10]

$$K_p = \frac{2\pi f_c (L_1 + L_2)}{H_{i2} K_{\text{PWM}}}. \tag{21}$$

To minimize the phase contribution of the PR regulator at the crossover frequency, its corner frequency (i.e., $2K_r\omega_i/(2\pi K_p)$) is usually set a decade below f_c [36]. Thus, the resonant gain K_{r} is calculated as

$$K_r = \frac{2\pi f_c}{10} \cdot \frac{K_p}{2\omega_i}. \tag{22}$$

From (21) and (22), it is clear that K_p and K_r can be solely determined once f_c is specified. Generally, the maximum achievable value for f_c is limited by the requirement of PM [36]. As reported in [43], $f_c \asymp 4\% f_s$ (i.e., 0.8 kHz in the test system) with a PM over 60° is expected to achieve a small percentage overshoot (PO). Substituting f_c = 0.8 kHz into (21) and then (22), K_p = 0.32 and K_r = 25 are yielded. In practice, the PR regulator is decomposed into two simple integrators, where the direct integrator is discretized by forward difference and the feedback one is discretized by backward difference [44], [45]. Thus, the discrete representation of $G_{\text{i}}(s)$ is obtained as

$$G_i(z) = K_p + \frac{2K_r\omega_i T_s (z - 1)}{z^2 + z(\omega_o^2 T_s^2 + 2\omega_i T_s - 2) - 2\omega_i T_s + 1}. \tag{23}$$

The capacitor-current-feedback function $H_{i1}(z)$ comes in two forms, which are either additionally introduced or inherently existent. As shown in Table I, in the two indirect current

control schemes, $G_i(z)$ is incorporated in $H_{i1}(z)$. Note that the resonant gain of the PR regulator mainly works nearby f_o and makes no contribution to the resonance damping. Hence, when tuning the damping term, the resonant gain of the PR regulator can be ignored, and $G_i(z)$ can be approximated as K_p [10], [24]. Accordingly, $H_{i1}(z)$ can be simplified as a constant coefficient H_{i1}, as shown in Table I. As reported in [29] and [33], H_{i1} should be designed to meet the gain margin requirements. To ensure system stability, the gain margins at f_r and $f_s/6$, which are, respectively, denoted by GM_1 and GM_2, need to be concerned. Moreover, the requirements on GM_1 and GM_2 vary with the relation between f_r and $f_s/6$. Specifically, if $f_r < f_s/6$, $\mathrm{GM}_1 > 0\,\mathrm{dB}$ and $\mathrm{GM}_2 < 0\,\mathrm{dB}$ are required; in contrast, if $f_r > f_s/6$, $\mathrm{GM}_1 < 0\,\mathrm{dB}$ and $\mathrm{GM}_2 > 0\,\mathrm{dB}$ are required. Substituting $G_i(z) = K_p$ and $H_{i1}(z) = H_{i1}$ into (8), the expressions of GM_1 and GM_2 in decibels can be obtained as

$$\mathrm{GM}_1 = -20\lg\left|T_{iL2}\left(e^{j\omega_r T_s}\right)\right| = 20\lg\frac{H_{i1}\left(L_1+L_2+L_g\right)}{H_{i2}K_pL_1} \tag{24a}$$

$$\begin{aligned}\mathrm{GM}_2 &= -20\lg\left|T_{iL2}\left(e^{j\pi/3}\right)\right| \\ &= 20\lg\left|\frac{L_1+L_2+L_g}{H_{i2}K_{\mathrm{PWM}}K_pL_1}\cdot\frac{H_{i1}K_{\mathrm{PWM}}\sin\omega_rT_s+\omega_rL_1\left(1-2\cos\omega_rT_s\right)}{\sin\omega_rT_s+\omega_rT_s\left(1-2\cos\omega_rT_s\right)}\right|.\end{aligned} \tag{24b}$$

For the test system shown in Table II, $f_r = 4.6\,\mathrm{kHz}$ and $f_s/6 = 3.3\,\mathrm{kHz}$, thus f_r is higher than $f_s/6$. However, with the increase of L_g, f_r will fall and cross over $f_s/6$. Under such a circumstance, the optimal H_{i1} is the one which yields $\mathrm{GM}_1 = \mathrm{GM}_2 = 0\,\mathrm{dB}$ for $f_r = f_s/6$ [33]. From (4), letting $f_r = f_s/6$, the critical L_g is calculated as $L_g = 220\,\mu\mathrm{H}$. Substituting $L_g = 220\,\mu\mathrm{H}$ and $K_p = 0.32$ into (24a) and letting $\mathrm{GM}_1 = 0\,\mathrm{dB}$, the optimal H_{i1} is calculated as $H_{i1} = 0.03$.

After a PR regulator and a general H_{i1} have been designed for all the three control schemes, the specific parameters (i.e., H_{i1a}, H_{i1b}, and β) in each control scheme can be obtained according to the relationships listed in Table I.

1) In the grid current control, $H_{i1} = H_{i1a}$, thus $H_{i1a} = 0.03$ is chosen.
2) In the inverter-side inductor current control, $H_{i1} = H_{i1b} + H_{i2}K_p$, where H_{i1b} is the additional damping and $H_{i2}K_p$ is the inherent one. If no additional damping is adopted (i.e., $H_{i1b} = 0$), then substituting $H_{i1} = H_{i2}K_p$ into (24a), GM_1 can be rewritten as

$$\mathrm{GM}_1\big|_{H_{i1}=H_{i2}K_p} = 20\lg\frac{L_1+L_2+L_g}{L_1} > 0\,\mathrm{dB}. \tag{25}$$

From (25), it can be observed that GM_1 is always greater than 0 dB. This is desirable for $f_r < f_s/6$, but goes against the requirement of $\mathrm{GM}_1 < 0\,\mathrm{dB}$ for $f_r > f_s/6$. Therefore, when i_{L1} is controlled, the inherent damping $H_{i2}K_p$ is helpful for $f_r < f_s/6$; but for $f_r > f_s/6$, the inherent damping $H_{i2}K_p$ is too large, and an additional positive feedback of the capacitor current (i.e., $H_{i1b} < 0$) is required to alleviate the overall damping. This explains the mechanism of the positive feedback of capacitor current in [28], and shows a new feature of the inherent damping in digital control. Substituting $K_p = 0.32$ and $H_{i1} = 0.03$ into $H_{i1} = H_{i1b} + H_{i2}K_p$, the desired H_{i1b} is calculated as $H_{i1b} = -0.018$.

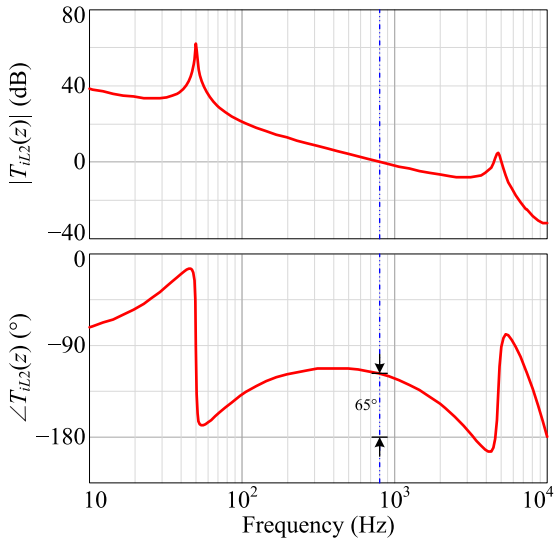

Fig. 7. Bode diagram of the loop gain $T_{iL2}(z)$ under $L_g = 0$.

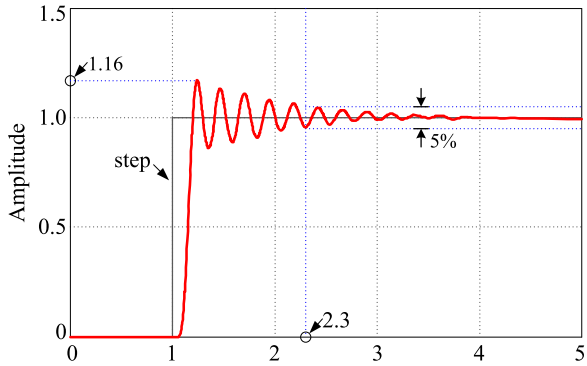

Fig. 8. Transient responses to a step input.

3) In the weighted average current control, $H_{i1} = \beta H_{i2}K_p$, and substituting it into (24a), GM_1 can be rewritten as

$$\mathrm{GM}_1\big|_{H_{i1}=\beta H_{i2}K_p} = 20\lg\left(\beta\cdot\frac{L_1+L_2+L_g}{L_1}\right). \tag{26}$$

From (26), it can be found that GM_1 is equal to 0 dB for $\beta = L_1/(L_1+L_2+L_g)$, which proves that i_{L2} is critically stable once again. In order to stabilize the grid current, the weight value β must be modified. Substituting $K_p = 0.32$ and $H_{i1} = 0.03$ into $H_{i1} = \beta H_{i2}K_p$, the desired β is calculated as $\beta = 0.625$ (recalling Table II, $L_1/(L_1+L_2+L_g) = 0.8$ under $L_g = 0$). In the following, the modified $\beta = 0.625$ will be compared to the conventional $\beta = 0.8$ to show its improvement.

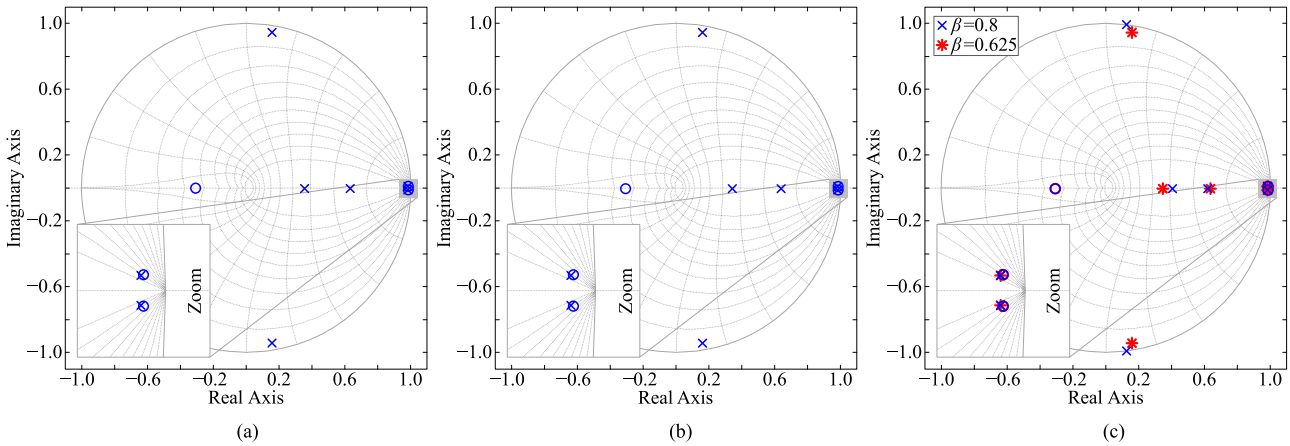

Fig. 9. Closed-loop pole-zero maps of i_{L2} under $L_g = 0$. (a) Grid current control. (b) Inverter-side inductor current control. (c) Weighted average current control.

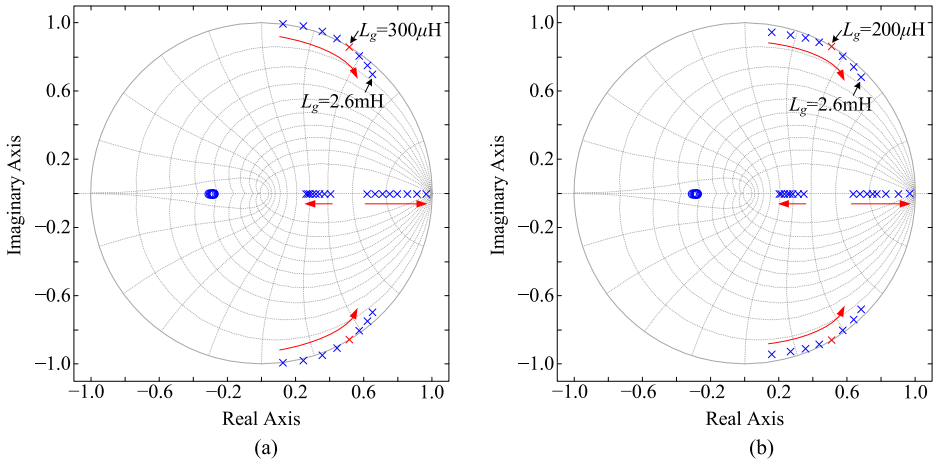

Fig. 10. Closed-loop pole-zero maps of i_{L2} with weighted average current control under the grid-impedance variation. (a) $\beta = 0.8$. (b) $\beta = 0.625$.

Based on the designed controller parameters, the Bode diagram of the loop gain $T_{iL2}(z)$ under $L_g = 0$ is shown in Fig. 7, where $f_c = 0.8$ kHz and PM $= 65°$ can be readily identified, and the transient response to a step input, which is the same as a step change in the rotating reference frame, is shown in Fig. 8. It is clear to see that the PO is 16% and the settling time $t_{5\%}$ is 1.3 ms (with a tolerance band of 5%), which indicate a satisfactory dynamic performance.

According to the closed-loop transfer function $T_{iL2}(z)/[1 + T_{iL2}(z)]$, the closed-loop pole-zero maps of i_{L2} can be drawn using MATLAB. Fig. 9 shows those maps under $L_g = 0$. To achieve a detailed observation, the pairs of closed-loop poles and zeros introduced by the PR regulator are zoomed in at the lower-left corner. For the grid current control with $H_{i1a} = 0.03$ and the inverter-side inductor current control with $H_{i1b} = -0.018$, the pole-zero locations are almost the same since they are designed with matched loop gain $T_{iL2}(z)$, as shown in Fig. 9(a) and (b). In the weighted average current control, two different β are evaluated, as shown in Fig. 9(c). For $\beta = 0.8$, a pair of resonant poles exactly locates at the unit circle, which verifies the analysis in Section III-B that i_{L2} is critically stable. For $\beta = 0.625$, the pole-zero location is the same as Fig. 9(a) and (b) due to the matched loop gain $T_{iL2}(z)$.

Fig. 10 shows the closed-loop pole-zero maps of i_{L2} with L_g varying up to 2.6 mH (the pairs of closed-loop poles and zeros introduced by the PR regulator are not shown here since they vary a little). Note that the three current control schemes have a similar pole-zero location with matched loop gain $T_{iL2}(z)$. The pole-zero map in the weighted average current control is taken as an instance. For $\beta = 0.8$, as shown in Fig. 10(a), the resonant poles first move outside the unit circle for $L_g < 300\,\mu$H, and then track back inside with the further increase of L_g. For $\beta = 0.625$, as shown in Fig. 10(b), the resonant poles are damped into the unit circle except for $L_g = 220\,\mu$H (i.e., $f_r = f_s/6$, where the resonant poles exactly locate at the unit circle). Thus, stable operations are retained for all L_g except 220 μH, and it is critically stable for $L_g = 220\,\mu$H. In practice, due to the damping effect of the parasitic resistors, a stable operation will be also preserved for $L_g = 220\,\mu$H.

V. Experimental Verification

A 6-kW prototype, as shown in Fig. 11, is built and tested in the lab. The single-phase inverter bridge is implemented using two IGBT modules (CM100DY-24NF). These modules are driven by M57962L. The PCC voltage v_g', which is used in the

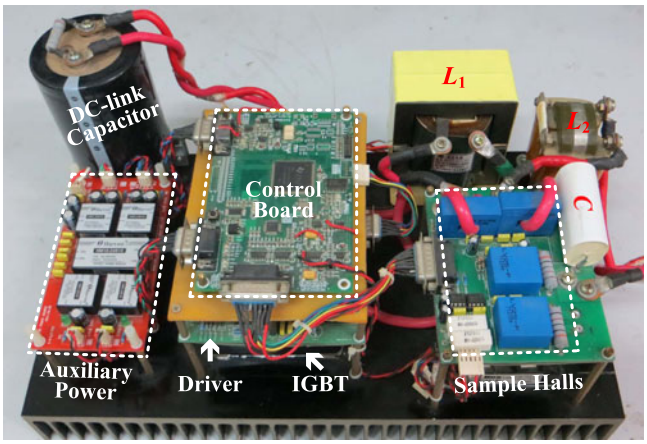

Fig. 11. Photograph of the single-phase grid-connected inverter prototype.

PLL, is sensed by a voltage hall (LV25-P). The inverter-side inductor current i_{L1} and the grid current i_{L2} are separately sensed by two current halls (LA55-P), and the difference between them is calculated as the capacitor current i_C. The controller is implemented in a TI TMS320F2812 DSP.

Figs. 12 and 13 show the experimental results with the grid current control and the inverter-side inductor current control, respectively. Both control schemes are evaluated under $L_g = 0$. $H_{i1a} = 0.03$ and $H_{i1b} = -0.018$ are selected for these two control schemes. The experimental waveforms when the current reference steps between half and full loads are given in Figs. 12(a) and 13(a). To achieve a detailed observation, the waveforms when the current reference steps downward are zoomed in, as shown in Figs. 12(b) and 13(b). The PO [σ/ $I_{\rm st}$ in Figs. 12(b) and 13(b)] and the settling time $t_{5\%}$ of i_{L2} are measured as 12% and 0.5 ms in both control schemes. Because of the effects of the dead time and parasitic resistors, the measured transient responses are better than the simulation results. As discussed in Section IV, when i_{L1} is controlled for $f_r > f_s/6$, instability will arise without an additional damping (i.e., $H_{i1b} = 0$). Recalling Table I, $H_{i1b} = 0$ corresponds to $H_{i1} = H_{i1a} = 0.048$. When H_{i1a} is changed from 0.03 to 0.048 and H_{i1b} is changed from -0.018 to 0, severe oscillation arises and tends to increase in both i_{L1} and i_{L2}, as shown in Figs. 12(c) and 13(c). This indicates instability and is consistent with the analysis in Section IV. Figs. 12(d) and 13(d) give the zoomed-in waveforms over a fundamental period, from which the oscillation frequency is measured as 4.6 kHz, which is exactly the *LCL*-filter resonance frequency. The experimental results show that if different control schemes are designed with matched loop gain $T_{iL2}(z)$, their control performances and stabilities will be the same.

Fig. 14 shows the experimental results with the weighted average current control under $L_g = 0$. For $\beta = 0.8$, the experimental waveform when the current reference steps from full to half loads is given in Fig. 14(a). It can be observed that although $i_{\rm WA}$ exhibits satisfactory steady-state and dynamic performances, i_{L1} and i_{L2} are both critically stable. When the current reference steps downward, both i_{L1} and i_{L2} oscillate, and the oscillation decays very slowly and lasts for a long time (more than two fundamental periods). Fig. 14(b) gives the zoomed-in

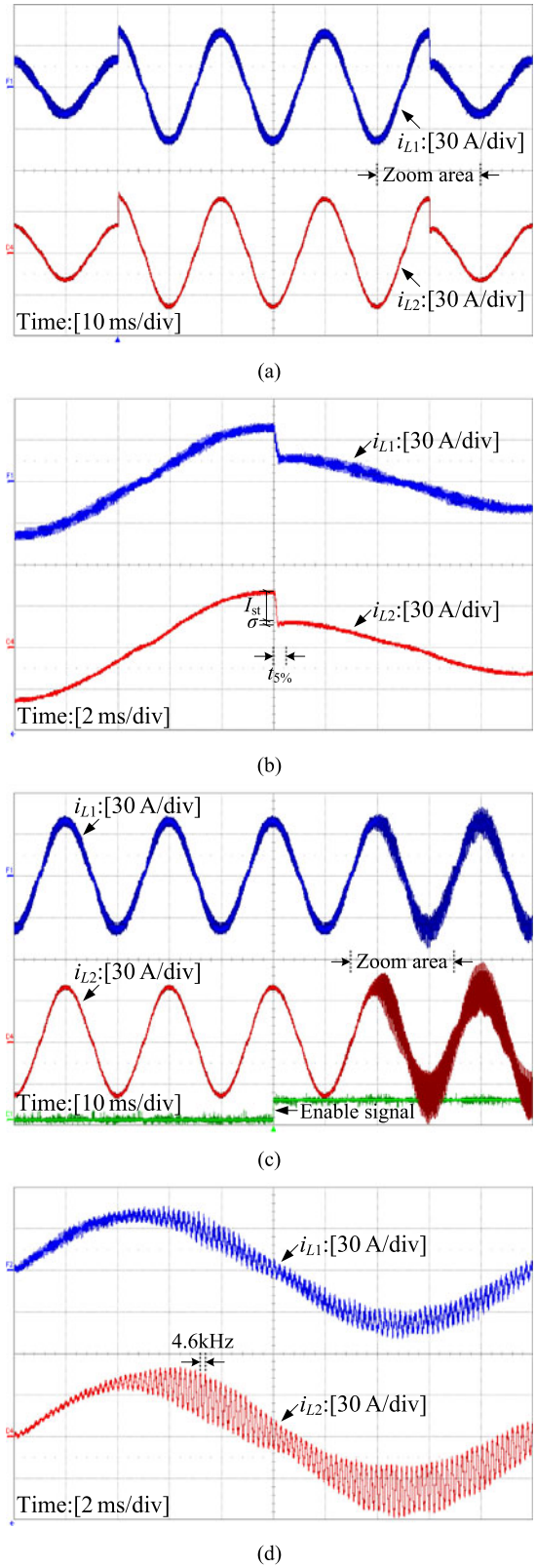

Fig. 12. Experimental results with grid current control under $L_g = 0$. (a) $H_{i1a} = 0.03$, and the current reference steps between half and full loads. (b) Zoom of (a). (c) $H_{i1a} = 0.03$ at first and is changed to $H_{i1a} = 0.048$ at the rising edge of the enable signal. (d) Zoom of (c).

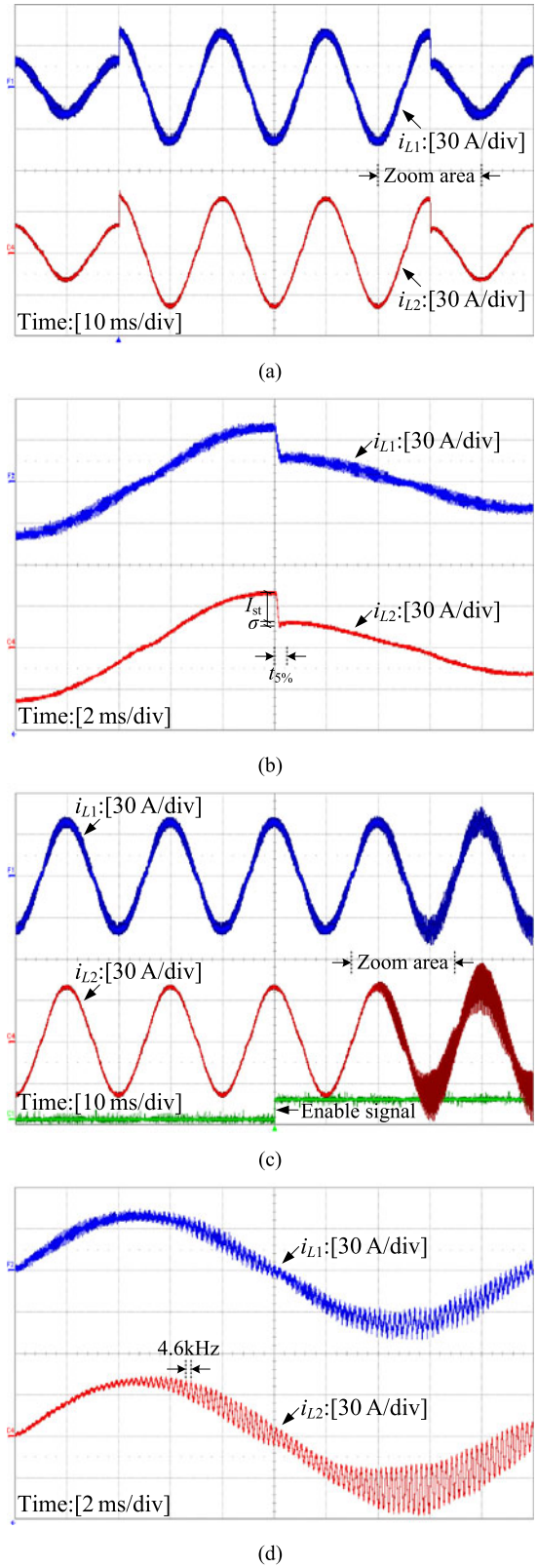

Fig. 13. Experimental results with inverter-side inductor current control under $L_g = 0$. (a) $H_{i1b} = -0.018$, and the current reference steps between half and full loads. (b) Zoom of (a). (c) $H_{i1b} = -0.018$ at first and is changed to $H_{i1b} = 0$ at the rising edge of the enable signal. (d) Zoom of (c).

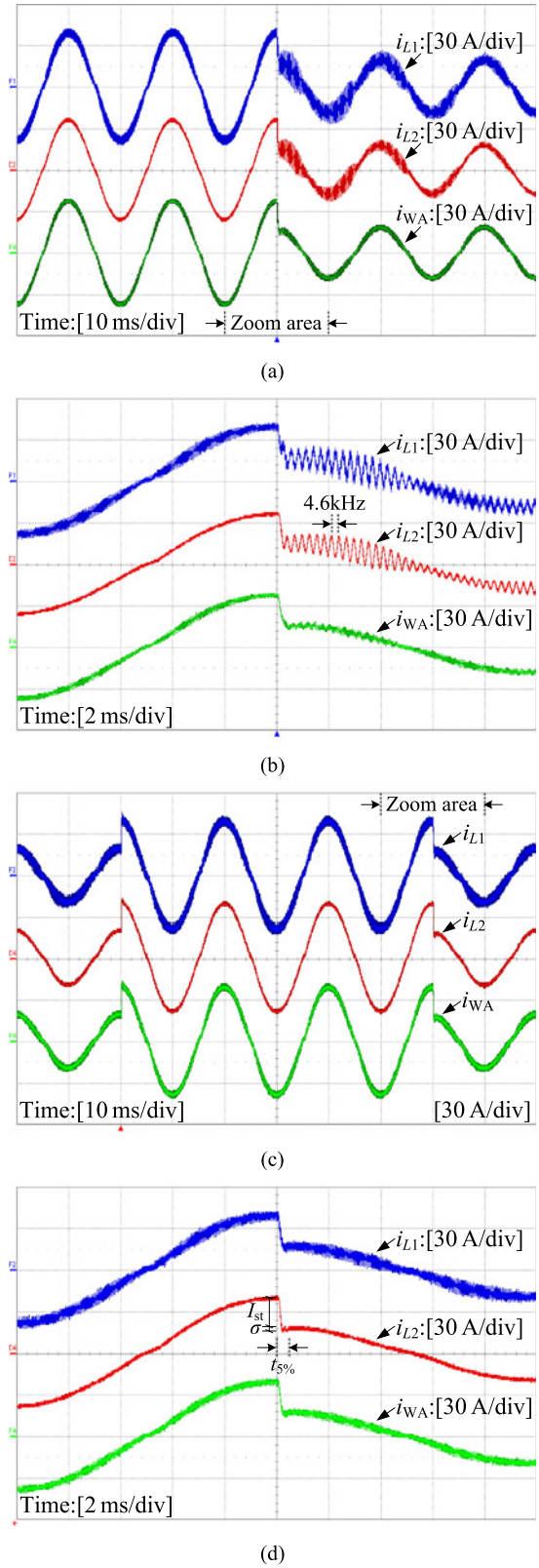

Fig. 14. Experimental results with weighted average current control under $L_g = 0$. (a) $\beta = 0.8$, and the current reference steps from full to half loads. (b) Zoom of (a). (c) $\beta = 0.625$, and the current reference steps between half and full loads. (d) Zoom of (c).

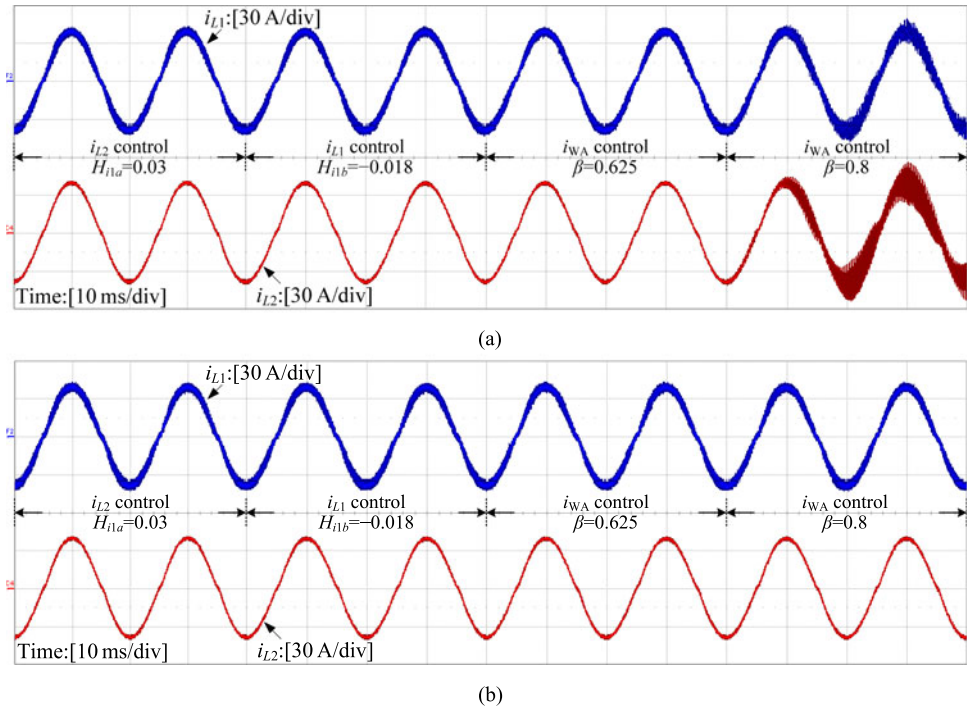

Fig. 15. Experimental results with different control schemes under the grid-impedance variation. (a) $L_g = 220\,\mu$H. (b) $L_g = 2.6$ mH.

waveform over a fundamental period, from which the oscillation frequency is measured as 4.6 kHz. For $\beta = 0.625$, the experimental waveform when the current reference steps between half and full loads is given in Fig. 14(c). It can be observed that the current oscillation disappears, and the dynamic performance is substantially improved for both i_{L1} and i_{L2}. Fig. 14(d) gives the zoomed-in waveform when the current reference steps downward. The PO [σ/ $I_{\rm st}$ in Fig. 14(d)] and the settling time $t_{5\%}$ of i_{L2} are measured as 12% and 0.5 ms, respectively, which are consistent with Figs. 12(b) and 13(b). The experimental results show that when the weighted average current is controlled, the weight value β should be modified according to the desired damping to improve the grid current stability.

Fig. 15 shows the experimental results with different control schemes under the grid-impedance variation. Both $L_g = 220\,\mu$H (the worst case) and $L_g = 2.6\,m$H are tested here. For $L_g = 220\mu$H, as shown in Fig. 15(a), a stable operation is retained in any of the grid current control with H_{i1a} = 0.03, the inverter-side inductor current control with H_{i1b} = - 0.018, and the weighted average current control with $\beta = 0.625$. However, when it is changed to the weighted average current control with $\beta = 0.8$, disastrous oscillation is triggered. For L_g = 2.6 mH, as shown in Fig. 15(b), satisfactory stable operation is performed in all the above four cases, which is consistent with the design result in Section IV. The experimental results show that with the optimal H_{i1} = 0.03, strong robustness is ensured in different control schemes.

VI. Conclusion

For the *LCL*-type grid-connected inverter, a general mathematical model is built in this paper to describe the three current control schemes, which are the grid current control, the inverter-side inductor current control, and the weighted average current control. This model takes the grid current as the equivalent target control variable, the capacitor current feedback as the damping solution, and accounts for the computation and PWM delays. Based on the general mathematical model, deep insights into the relationships among different control schemes can be drawn, and stability analysis from the perspective of grid current is presented. It reveals that when the inverter-side inductor current is controlled, the grid current shows the same stability as the inverter-side inductor current; but when the weighted average current is controlled, both the grid current and the inverter-side inductor current are critically stable even though the weighted average current can be easily stabilized. Moreover, a unified controller design, which takes account of the grid-impedance variation, is proposed using the general mathematical model. In this way, the mechanism of the positive feedback of capacitor current is well explained in the inverter-side inductor current control, and a modified weight value is easily selected in the weighted average current control to stabilize the grid current. Experimental results from a 6-kW prototype confirm the theoretical expectations.

Appendix

In this appendix, the discrete loop gains $T_{iL1}(z)$, $T_{i\rm WA}(z)$, and $T_{iL2}(z)$ are derived. Referring to Fig. 2(a), the transfer functions from the inverter bridge output voltage $v_{\rm inv}(s)$ to the capacitor current $i_C(s)$, the grid current $i_{L2}(s)$, and the inverter-side inductor current $i_{L1}(s)$ can be derived as

$$G_{iC}(s) = \frac{i_C(s)}{v_{\rm inv}(s)} = \frac{1}{sL_1} \cdot \frac{s^2}{s^2 + \omega_r^2}$$

$$T_{iL1}(z) = \frac{H_{i2}K_{\mathrm{PWM}}G_i(z)G_{iL1}(z)}{z + H_{i1b}K_{\mathrm{PWM}}G_{iC}(z)}$$
$$= \frac{H_{i2}K_{\mathrm{PWM}}G_i(z)}{\omega_r L_1(L_1+L_2+L_g)} \cdot \frac{\omega_r L_1 T_s\left(z^2 - 2z\cos\omega_r T_s + 1\right) + (z-1)^2(L_2+L_g)\sin\omega_r T_s}{(z-1)\left[z\left(z^2 - 2z\cos\omega_r T_s + 1\right) + \frac{H_{i1b}K_{\mathrm{PWM}}}{\omega_r L_1}(z-1)\sin\omega_r T_s\right]} \quad \text{(A3)}$$

$$T_{i\mathrm{WA}}(z) = H_{i2}K_{\mathrm{PWM}}z^{-1}G_i(z)\left[\beta G_{iL1}(z) + (1-\beta)G_{iL2}(z)\right]$$
$$= \frac{H_{i2}K_{\mathrm{PWM}}G_i(z)}{\omega_r L_1(L_1+L_2+L_g)} \cdot \frac{\omega_r L_1 T_s\left(z^2 - 2z\cos\omega_r T_s + 1\right) + (z-1)^2\left[\beta(L_1+L_2+L_g) - L_1\right]\sin\omega_r T_s}{z(z-1)\left(z^2 - 2z\cos\omega_r T_s + 1\right)} \quad \text{(A4)}$$

$$T_{iL2}(z) = \frac{H_{i2}K_{\mathrm{PWM}}G_i(z)G_{iL2}(z)}{z + K_{\mathrm{PWM}}H_{i1}(z)G_{iC}(z)}$$
$$= \frac{H_{i2}K_{\mathrm{PWM}}G_i(z)}{\omega_r(L_1+L_2+L_g)} \cdot \frac{\omega_r T_s\left(z^2 - 2z\cos\omega_r T_s + 1\right) - (z-1)^2\sin\omega_r T_s}{(z-1)\left[z\left(z^2 - 2z\cos\omega_r T_s + 1\right) + \frac{K_{\mathrm{PWM}}\sin\omega_r T_s}{\omega_r L_1}(z-1)H_{i1}(z)\right]} \quad \text{(A5)}$$

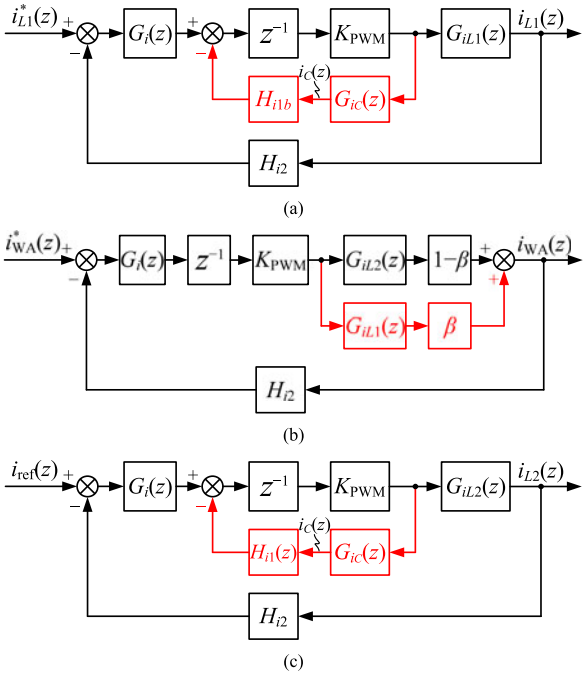

Fig. A1. Equivalent discrete-time models of (a) Fig. 2(b), (b) Fig. 2(c), and (c) Fig. 4.

$$G_{iL2}(s) = \frac{i_{L2}(s)}{v_{\mathrm{inv}}(s)} = \frac{1}{s(L_1+L_2+L_g)} \cdot \frac{\omega_r^2}{s^2+\omega_r^2}$$
$$G_{iL1}(s) = \frac{i_{L1}(s)}{v_{\mathrm{inv}}(s)} = \frac{1}{sL_1} \cdot \frac{s^2}{s^2+\omega_r^2} + \frac{1}{s(L_1+L_2+L_g)} \cdot \frac{\omega_r^2}{s^2+\omega_r^2}. \quad \text{(A1)}$$

Applying the ZOH transform to $G_{iC}(s)$, $G_{iL2}(s)$, and $G_{iL1}(s)$ yields

$$G_{iC}(z) = Z_{\mathrm{ZOH}}\left[G_{iC}(s)\right] = \frac{\sin\omega_r T_s}{\omega_r L_1} \cdot \frac{z-1}{z^2 - 2z\cos\omega_r T_s + 1}$$

$$G_{iL2}(z) = Z_{\mathrm{ZOH}}\left[G_{iL2}(s)\right] = \frac{T_s}{(L_1+L_2+L_g)(z-1)} - \frac{\sin\omega_r T_s}{\omega_r(L_1+L_2+L_g)} \cdot \frac{z-1}{z^2 - 2z\cos\omega_r T_s + 1}$$
$$G_{iL1}(z) = Z_{\mathrm{ZOH}}\left[G_{iL1}(s)\right] = \frac{T_s}{(L_1+L_2+L_g)(z-1)} + \frac{(L_2+L_g)\sin\omega_r T_s}{\omega_r L_1(L_1+L_2+L_g)} \cdot \frac{z-1}{z^2 - 2z\cos\omega_r T_s + 1}. \quad \text{(A2)}$$

Ignoring the grid voltage disturbance, the mathematical models in Fig. 2(b) and (c) and Fig. 4 are transformed into the discrete ones, as shown in Fig. A1. From Fig. A1, the loop gains can be obtained as equation (A3)–(A5) as shown at the top of the page.

REFERENCES

[1] F. Blaabjerg, R. Teodorescu, M. Liserre, and A. V. Timbus, "Overview of control and grid synchronization for distributed power generation systems," *IEEE Trans. Ind. Electron.*, vol. 53, no. 5, pp. 1398–1409, Oct. 2006.

[2] J. He and Y. W. Li, "Generalized closed-loop control schemes with embedded virtual impedances for voltage source converters with *LC* or *LCL* filters," *IEEE Trans. Power Electron.*, vol. 27, no. 4, pp. 1850–1861, Apr. 2012.

[3] R. P. Alzola, M. Liserre, F. Blaabjerg, R. Sebastián, J. Dannehl, and F. W. Fuchs, "Analysis of the passive damping losses in *LCL*-filter-based grid converters," *IEEE Trans. Power Electron.*, vol. 28, no. 6, pp. 2642–2646, Jun. 2013.

[4] R. N. Beres, X. Wang, F. Blaabjerg, M. Liserre, and C. L. Bak, "Optimal design of high-order passive-damped filters for grid-connected applications," *IEEE Trans. Power Electron.*, vol. 31, no. 3, pp. 2083–2098, Mar. 2016.

[5] R. N. Beres, X. Wang, M. Liserre, F. Blaabjerg, and C. L. Bak, "A review of passive power filters for three-phase grid connected voltage-source converters," *IEEE J. Emerg. Sel. Topics Power Electron.*, vol. 4, no. 1, pp. 54–69, Mar. 2016.

[6] J. Dannehl, C. Wessels, and F. W. Fuchs, "Filter-based active damping of voltage source converters with *LCL* filter," *IEEE Trans. Ind. Electron.*, vol. 58, no. 8, pp. 3623–3633, Aug. 2011.

[7] L. Harnefors, A. G. Yepes, A. Vidal, and J. D. Gandoy, "Passivity-based stabilization of voltage-source converters equipped with *LCL* input filters," in *Proc. 40th Annu. Conf. IEEE Ind. Electron. Soc.*, 2014, pp. 1700–1706.

[8] Z. Xin, P. C. Loh, X. Wang, F. Blaabjerg, and Y. Tang, "Highly accurate derivatives for *LCL*-filtered grid converter with capacitor voltage active

damping," *IEEE Trans. Power Electron.*, vol. 31, no. 5, pp. 3612–3625, May 2016.
[9] L. Harnefors, L. Zhang, and M. Bongiorno, "Frequency-domain passivity-based current controller design," *IET Power Electron*., vol. 1, no. 4, pp. 455–465, Dec. 2008.
[10] C. Bao, X. Ruan, X. Wang, W. Li, D. Pan, and K. Weng, "Step-by-step controller design for *LCL*-type grid-connected inverter with capacitor-current- feedback active-damping," *IEEE Trans. Power Electron.*, vol. 29, no. 3, pp. 1239–1253, Mar. 2014.
[11] M. Huang, X. Wang, P. C. Loh, and F. Blaabjerg, "Active damping of *LLCL*-filter resonance based on *LC*-trap voltage or current feedback," *IEEE Trans. Power Electron.*, vol. 31, no. 3, pp. 2337–2346, Mar. 2016.
[12] Y. Jia, J. Zhao, and X. Fu, "Direct grid current control of *LCL*-filtered grid-connected inverter mitigating grid voltage disturbance," *IEEE Trans. Power Electron.*, vol. 29, no. 3, pp. 1532–1541, Mar. 2014.
[13] Z. Zou, Z. Wang, and M. Cheng, "Modeling, analysis, and design of multifunction grid-interfaced inverters with output *LCL* filter," *IEEE Trans. Power Electron.*, vol. 29, no. 7, pp. 3830–3839, Jul. 2014.
[14] X. Wang, F. Blaabjerg, and P. C. Loh, "Grid-current-feedback active damping for *LCL* resonance in grid-connected voltage source converters," *IEEE Trans. Power Electron.*, vol. 31, no. 1, pp. 213–223, Jan. 2016.
[15] J. Dannehl, C. Wessels, and F. W. Fuchs, "Limitations of voltage-oriented PI current control of grid-connected PWM rectifiers with *LCL* filters," *IEEE Trans. Ind. Electron.*, vol. 56, no. 2, pp. 380–388, Feb. 2009.
[16] J. Dannehl, F. W. Fuchs, and P. B. Thøgersen, "PI state space current control of grid-connected PWM converters with *LCL* filters," *IEEE Trans. Power Electron.*, vol. 25, no. 9, pp. 2320–2330, Sep. 2010.
[17] R. P. Alzola, M. Liserre, F. Blaabjerg, M. Ordonez, and T. Kerekes, "A self-commissioning notch filter for active damping in a three-phase *LCL*-filter- based grid-tie converter," *IEEE Trans. Power Electron.*, vol. 29, no. 12, pp. 6754–6761, Dec. 2014.
[18] G. Shen, D. Xu, L. Cao, and X. Zhu, "An improved control strategy for grid-connected voltage source inverters with an *LCL* filter," *IEEE Trans. Power Electron.*, vol. 23, no. 4, pp. 1899–1906, Jul. 2008.
[19] G. Shen, X. Zhu, J. Zhang, and D. Xu, "A new feedback method for PR current control of *LCL*-filter-based grid-connected inverter," *IEEE Trans. Ind. Electron.*, vol. 57, no. 6, pp. 2033–2041, Jun. 2010.
[20] N. He, D. Xu, Y. Zhu, J. Zhang, G. Shen, Y. Zhang, J. Ma, and C. Liu, "Weighted average current control in a three-phase grid inverter with an *LCL* filter," *IEEE Trans. Power Electron.*, vol. 28, no. 6, pp. 2785–2797, Jun. 2013.
[21] L. Harnefors, A. G. Yepes, A. Vidal, and J. D. Gandoy, "Passivity-based stabilization of resonant current controllers with consideration of time delay," *IEEE Trans. Power Electron.*, vol. 29, no. 12, pp. 6260–6263, Dec. 2014.
[22] L. Harnefors, A. G. Yepes, A. Vidal, and J. D. Gandoy, "Passivity-based controller design of grid-connected VSCs for prevention of electrical resonance instability," *IEEE Trans. Ind. Electron.*, vol. 62, no. 2, pp. 702–710, Feb. 2015.
[23] L. Harnefors, X. Wang, A. G. Yepes, and F. Blaabjerg, "Passivity-based stability assessment of grid-connected VSCs – an overview," *IEEE J. Emerg. Sel. Topics Power Electron.*, vol. 4, no. 1, pp. 116–125, Mar. 2016.
[24] S. G. Parker, B. P. McGrath, and D. G. Holmes, "Regions of active damping control for *LCL* filters," *IEEE Trans. Ind. Appl.*, vol. 50, no. 1, pp. 424–432, Jan./Feb. 2014.
[25] C. Zou, B. Liu, S. Duan, and R. Li, "Influence of delay on system stability and delay optimization of grid-connected inverters with *LCL* filter," *IEEE Trans. Ind. Informat.*, vol. 10, no. 3, pp. 1775–1784, Aug. 2014.
[26] J. Wang, J. D. Yan, L. Jiang, and J. Zou, "Delay-dependent stability of single-loop controlled grid-connected inverters with *LCL* filters," *IEEE Trans. Power Electron.*, vol. 31, no. 1, pp. 743–757, Jan. 2016.
[27] M. Liserre, R. Teodorescu, and F. Blaabjerg, "Stability of photovoltaic and wind turbine grid-connected inverters for a large set of grid impedance values," *IEEE Trans. Power Electron.*, vol. 21, no. 1, pp. 263–272, Jan. 2006.
[28] J. Dannehl, F. W. Fuchs, S. Hansen, and P. B. Thøgersen, "Investigation of active damping approaches for PI-based current control of grid-connected pulse width modulation converters with *LCL* filters," *IEEE Trans. Ind. Appl.*, vol. 46, no. 4, pp. 1509–1517, Jul./Aug. 2010.
[29] D. Pan, X. Ruan, C. Bao, W. Li, and X. Wang, "Capacitor-current-feedback active damping with reduced computation delay for improving robustness of *LCL*-type grid-connected inverter," *IEEE Trans. Power Electron.*, vol. 29, no. 7, pp. 3414–3427, Jul. 2014.
[30] D. Yang, X. Ruan, and H. Wu, "A real-time computation method with dual sampling mode to improve the current control performance of the *LCL*-type grid-connected inverter," *IEEE Trans. Ind. Electron.*, vol. 62, no. 7, pp. 4563–4572, Jul. 2015.
[31] X. Wang, F. Blaabjerg, and P. C. Loh, "Virtual *RC* damping of *LCL*-filtered voltage source converters with extended selective harmonic compensation," *IEEE Trans. Power Electron.*, vol. 30, no. 9, pp. 4726–4737, Sep. 2015.
[32] X. Li, X. Wu, Y. Geng, X. Yuan, C. Xia, and X. Zhang, "Wide damping region for *LCL*-type grid-connected inverter with an improved capacitor-current- feedback method," *IEEE Trans. Power Electron.*, vol. 30, no. 9, pp. 5247–5259, Sep. 2015.
[33] D. Pan, X. Ruan, C. Bao, W. Li, and X. Wang, "Optimized controller design for *LCL*-type grid-connected inverter to achieve high robustness against grid-impedance variation," *IEEE Trans. Ind. Electron.*, vol. 62, no. 3, pp. 1537–1547, Mar. 2015.
[34] G. C. Goodwin, S. F. Graebe, and M. E. Salgado, *Control System Design*. Upper Saddle River, NJ, USA: Prentice-Hall, 2000.
[35] F. Huerta, D. Pizarro, S. Cóbreces, F. J. Rodríguez, C. Girón, and A. Rodríguez, "LQG servo controller for the current control of *LCL* grid-connected voltage-source converters," *IEEE Trans. Ind. Electron.*, vol. 59, no. 11, pp. 4272–4284, Nov. 2012.
[36] D. G. Holmes, T. A. Lipo, B. P. McGrath, and W. Y. Kong, "Optimized design of stationary frame three phase AC current regulators," *IEEE Trans. Power Electron.*, vol. 24, no. 11, pp. 2417–2426, Nov. 2009.
[37] D. G. Holmes, B. P. McGrath, and S. G. Parker, "Current regulation strategies for vector-controlled induction motor drives," *IEEE Trans. Ind. Electron.*, vol. 59, no. 10, pp. 3680–3689, Oct. 2012.
[38] B. P. McGrath, S. G. Parker, and D. G. Holmes, "High performance current regulation for low-pulse-ratio inverters," *IEEE Trans. Ind. Appl.*, vol. 49, no. 1, pp. 149–158, Jan./Feb. 2013.
[39] Y. Tang, P. C. Loh, P. Wang, F. H. Choo, and F. Gao, "Exploring inherent damping characteristic of *LCL*-filters for three-phase grid-connected voltage source inverters," *IEEE Trans. Power Electron.*, vol. 27, no. 3, pp. 1433–1443, Mar. 2012.
[40] W. Wu, Y. He, and F. Blaabjerg, "An *LLCL* power filter for single-phase grid-tied inverter," *IEEE Trans. Power Electron.*, vol. 27, no. 2, pp. 782–789, Feb. 2012.
[41] Y. Tang, P. C. Loh, P. Wang, F. H. Choo, F. Gao, and F. Blaabjerg, "Generalized design of high performance shunt active power filter with output *LCL* filter," *IEEE Trans. Ind. Electron.*, vol. 59, no. 3, pp. 1443–1452, Mar. 2012.
[42] D. Pan, X. Ruan, C. Bao, W. Li, and X. Wang, "Magnetic integration of the *LCL* filter in grid-connected inverters," *IEEE Trans. Power Electron.*, vol. 29, no. 4, pp. 1573–1578, Apr. 2014.
[43] A. G. Yepes, A. Vidal, J. Malvar, O. López, and J. D.-Gandoy, "Tuning method aimed at optimized settling time and overshoot for synchronous proportional-integral current control in electric machines," *IEEE Trans. Power Electron.*, vol. 29, no. 6, pp. 3041–3054, Jun. 2014.
[44] A. G. Yepes, F. D. Freijedo, J. D. Gandoy, Ó. López, J. Malvar, and P. F. Comesaña, "Effects of discretization methods on the performance of resonant controllers," *IEEE Trans. Power Electron.*, vol. 25, no. 7, pp. 1692–1712, Jul. 2010.
[45] A. G. Yepes, F. D. Freijedo, Ó. López, and J. D.-Gandoy, "High-performance digital resonant controllers implemented with two integrators," *IEEE Trans. Power Electron.*, vol. 26, no. 2, pp. 563–576, Feb. 2011.

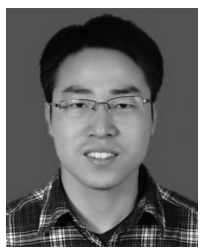

Donghua Pan (S'12–M'15) was born in Hubei Province, China, in 1987. He received the B.S. and Ph.D. degrees in electrical and electronic engineering from Huazhong University of Science and Technology, Wuhan, China, in 2010 and 2015, respectively.

He is currently a Research Engineer with Suzhou Inovance Technology, Co., Ltd., Suzhou, China. His research interests include magnetic integration technique and renewable energy generation system.

Xinbo Ruan (M'97–SM'02–F'16) was born in Hubei Province, China, in 1970. He received the B.S. and Ph.D. degrees in electrical engineering from Nanjing University of Aeronautics and Astronautics (NUAA), Nanjing, China, in 1991 and 1996, respectively.

In 1996, he joined the Faculty of Electrical Engineering Teaching and Research Division, NUAA, where he became a Professor with the College of Automation Engineering in 2002 and has been involved in teaching and research in the field of power electronics. From August to October 2007, he was a Research Fellow in the Department of Electronic and Information Engineering, Hong Kong Polytechnic University, Hong Kong, China. From 2008 to 2011, he was also with the School of Electrical and Electronic Engineering, Huazhong University of Science and Technology, Wuhan, China. He is currently a Guest Professor with Beijing Jiaotong University, Beijing, China, Hefei University of Technology, Hefei, China, and Wuhan University, Wuhan, China. He is the Author or Coauthor of seven books and more than 200 technical papers published in journals and conferences. His main research interests include soft-switching dc–dc converters, soft-switching inverters, power factor correction converters, modeling the converters, power electronics system integration, and renewable energy generation system.

Dr. Ruan received the Delta Scholarship by the Delta Environment and Education Fund in 2003 and the Special Appointed Professor of the Chang Jiang Scholars Program by the Ministry of Education, China, in 2007. From 2005 to 2013, he was the Vice President of the China Power Supply Society, and since 2014, he has been the Vice Chair of the Technical Committee on Renewable Energy Systems within the IEEE Industrial Electronics Society. He is currently an Associate Editor for the IEEE TRANSACTIONS ON INDUSTRIAL ELECTRONICS, the IEEE JOURNAL OF EMERGING AND SELECTED TOPICS IN POWER ELECTRONICS, the IEEE TRANSACTIONS ON POWER ELECTRONICS, and the IEEE TRANSACTIONS ON CIRCUITS AND SYSTEMS II: EXPRESS BRIEFS.

Xuehua Wang (M'12) was born in Hubei Province, China, in 1978. He received the B.S. degree in electrical engineering from Nanjing University of Technology, Nanjing, China, in 2001, and the M.S. and Ph.D. degrees in electrical engineering from Nanjing University of Aeronautics and Astronautics, Nanjing, in 2004 and 2008, respectively.

He is currently an Associate Professor with the School of Electrical and Electronic Engineering, Huazhong University of Science and Technology, Wuhan, China. His main research interests include multilevel inverter and renewable energy generation system.

Hui Yu was born in Hubei Province, China, in 1990. He received the B.S. and M.S. degrees in electrical engineering from Huazhong University of Science and Technology, Wuhan, China, in 2013 and 2016, respectively. He is currently working toward the Ph.D. degree at the Future Renewable Electric Energy Delivery and Management Systems Center, Department of Electrical and Computer Engineering, North Carolina State University, Raleigh, NC, USA.

His research interests include microgrid and distributed power generation system.

Zhongwei Xing was born in Henan Province, China, in 1990. He received the B.S. degree in electrical and electronic engineering from Huazhong University of Science and Technology, Wuhan, China, in 2012, where he is currently working toward the Ph.D. degree.

His current research interests include modular multilevel converter and dc/dc converter applied in HVdc grids.